

High-Temperature Magnetism as a Probe for Structural and Compositional Uniformity in Ligand-Capped Magnetite Nanoparticles

Yury V. Kolen'ko,^{*,†} Manuel Bañobre-López,[†] Carlos Rodríguez-Abreu,[†] Enrique Carbó-Argibay,[†] Francis Leonard Deepak,[†] Dmitri Y. Petrovykh,[†] M. Fátima Cerqueira,[‡] Saeed Kamali,[§] Kirill Kovnir,[§] Dmitry V. Shtansky,^{||} Oleg I. Lebedev,[⊥] and Jose Rivas[†]

[†]International Iberian Nanotechnology Laboratory, Braga 4715-330, Portugal

[‡]Center of Physics, University of Minho, Braga 4710-057, Portugal

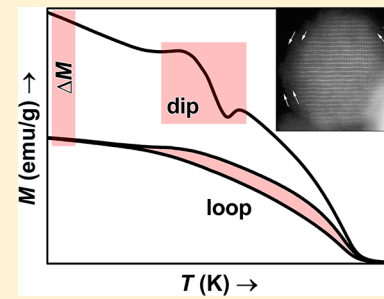
[§]Department of Chemistry, University of California, Davis, Davis California 95616, United States

^{||}National University of Science and Technology “MISIS”, Moscow, Russia

[⊥]Laboratoire CRISMAT, UMR 6508, CNRS-ENSICAEN, Caen 14050, France

Supporting Information

ABSTRACT: To investigate magnetostructural relationships in colloidal magnetite (Fe_3O_4) nanoparticles (NPs) at high temperature (300–900 K), we measured the temperature dependence of magnetization (M) of oleate-capped magnetite NPs ca. 20 nm in size. Magnetometry revealed an unusual irreversible high-temperature dependence of M for these NPs, with dip and loop features observed during heating–cooling cycles. Detailed characterizations of as-synthesized and annealed Fe_3O_4 NPs as well as reference ligand-free Fe_3O_4 NPs indicate that both types of features in $M(T)$ are related to thermal decomposition of the capping ligands. The ligand decomposition upon the initial heating induces a reduction of Fe^{3+} to Fe^{2+} and the associated dip in M , leading to more structurally and compositionally uniform magnetite NPs. Having lost the protective ligands, the NPs continually sinter during subsequent heating cycles, resulting in divergent M curves featuring loops. The increase in M with sintering proceeds not only through elimination of a magnetically dead layer on the particle surface, as a result of a decrease in specific surface area with increasing size, but also through an uncommonly invoked effect resulting from a significant change in $\text{Fe}^{3+}/\text{Fe}^{2+}$ ratio with heat treatment. The interpretation of irreversible features in $M(T)$ indicates that reversible $M(T)$ behavior, conversely, can be expected only for ligand-free, structurally and compositionally uniform magnetite NPs, suggesting a general applicability of high-temperature $M(T)$ measurements as an analytical method for probing the structure and composition of magnetic nanomaterials.



1. INTRODUCTION

Nanoparticles (NPs) of colloidal magnetite (Fe_3O_4) are a promising material for a wide range of biomedical applications, including magnetic resonance imaging, magnetic hyperthermia, magnetic separation/extraction, and drug delivery.¹ For these practical applications, Fe_3O_4 NPs with excellent magnetic properties can be produced as colloidal dispersions by wet-chemistry methods. As-synthesized NPs are typically functionalized with hydrophobic or hydrophilic capping ligands, thereby rendering them dispersible in organic or aqueous solvents, respectively.²

Surfaces of NPs strongly influence their magnetic properties (through surface/volume ratios). In particular, a reduced atomic moment at the surfaces of NPs lowers their saturation magnetization (M_s) relative to that of the corresponding bulk material. A reduction or even elimination of the surface disorder can be expected when capping ligands covalently bind to the NP surface; however, evidence for this putative surfactant effect is still a matter of debate. Although the

presence of surfactants has been shown to enhance M_s ,^{3,4} several studies have suggested that the presence of a surfactant does not cancel surface moment reduction but rather leads to glass-like behavior of surface spins.^{5,6}

Temperature-dependent measurements of nanoparticle magnetization [$M(T)$] could provide insights complementary to those obtained from the more typical measurements at or below room temperature, for example, by probing nanoscale compositional and structural features such as magnetic phase transitions, inhomogeneity, structural/point defects, nonstoichiometry, and cation ordering.⁷ For example, thermal treatment of ligand-capped Fe_3O_4 NPs can lead to chemical disproportionation of the magnetic phase, reduction of the surface, spin disarrangement, and annihilation of structural and point defects and can be detrimental to the chemical order.^{8–10}

Received: October 24, 2014

Revised: November 6, 2014

Published: November 6, 2014

These compositional and structural changes will affect the Fe–O–Fe superexchange interactions and thus be manifested in the modification of the magnetic properties at elevated temperatures. High-temperature magnetic measurements, therefore, can reveal useful information even for NPs that are intended primarily for room-temperature applications.

Previously, we observed a net reduction in M after high-temperature treatment of oleate- (OL^-) capped Fe_3O_4 NPs, which we attributed to spin disarrangement on the surface of the NPs resulting from thermal decomposition of the organic shells.¹¹ In this work, we found evidence of more complex mechanisms for temperature-dependent NP magnetic properties. Specifically, in heating–cooling cycles, our magnetite NPs exhibited irreversible M behavior with two peculiar effects, namely, dips and loops in their $M(T)$ curves, whose origins we investigated using several complementary characterization techniques.

2. EXPERIMENTAL SECTION

Colloidal magnetite NPs were prepared in aqueous reaction medium using a previously reported hydrothermal method;¹² the detailed synthesis procedure is described in the Supporting Information (SI). During synthesis, sodium oleate was used as a surfactant for the formation of OL-capped magnetite NPs, which are colloidally stable in organic solvents for long periods of time. To investigate their structural evolution with thermal treatment, as-synthesized OL-capped NPs (OL-HT) were annealed for 2 h at 650 and 900 K (OL-HT-650K and OL-HT-900K, respectively) under a static vacuum.

The NPs were characterized by magnetization measurements (SQUID-VSM magnetometer, Quantum Design), thermogravimetric analysis (TGA)/ differential scanning calorimetry (DSC) (TGA/DSC 1 STAR[®] system, Mettler-Toledo), powder X-ray diffraction (XRD) (XPert PRO diffractometer, PANalytical),¹³ Raman scattering (alpha300 R confocal microscope, WITec), transmission electron microscopy (TEM), high-resolution TEM (HRTEM), high-angle annular dark-field scanning TEM (HAADF-STEM), and energy-dispersive X-ray spectroscopy in STEM mode (STEM-EDX) [Tecnai G² 30 UT, Titan ChemiSTEM (FEI) and JEM-ARM200F (JEOL) microscopes], and ⁵⁷Fe Mössbauer spectroscopy.¹⁴ Detailed descriptions of NP characterization techniques are presented in the SI.

3. RESULTS

We began by considering the NP magnetic behavior $M(T)$ at elevated temperatures. We took advantage of a superconducting quantum interference device (SQUID) magnetometer to investigate $M(T)$ over the range of 300–900 K for the hydrothermally synthesized OL-capped OL-HT NPs (Figure 1). M is expressed in units of electromagnetic units per gram of iron oxide [emu/(g of iron oxide)]; that is, the mass was corrected for the ligand contribution determined by TGA. The $M(T)$ data were repeatedly recorded under an applied field of 10 kOe.

The most distinctive phenomenon in Figure 1 is the irreversible net loss of M , which is consistent with our previous observations.¹¹ Specifically, the OL-HT NPs exhibited a decrease in M when temperature was increased to the Curie temperature, T_C (black line, from A to B in Figure 1); M then continuously increased upon cooling from 900 to 300 K (black

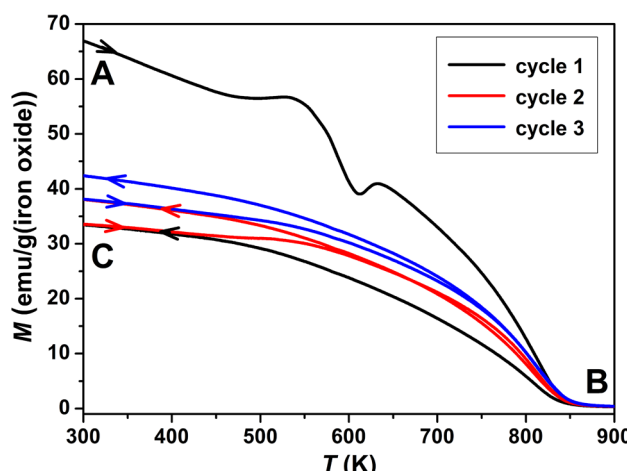


Figure 1. Three consecutive heating–cooling $M(T)$ cycles measured in a 10 kOe field for as-synthesized OL-HT magnetite NPs. $T_C \approx 840$ K.

line, from B to C in Figure 1), albeit with an irreversible net loss of M (ca. 50%) relative to the initial value.

Another interesting effect clearly observed for this sample is the dip in $M(T)$ upon the first heating (black line, from A to B in Figure 1); the temperature corresponding to the local minimum of the dip parameters, such as was found to be 602 K. No analogous dip features were found in the subsequent cooling or heating curves for this sample (Figure 1), indicating that the dip was an irreversible event, unique to the initial heating.

In addition to the dip in $M(T)$, OL-HT exhibited an irreversibility of the subsequent cooling and heating $M(T)$ curves, resulting in loop features. Figure 1 displays loops in $M(T)$ measured during three consecutive heating–cooling cycles: The temperature at which the curves diverged, the area of the loop, and M values all underwent substantial changes during the measurements. The area of the loop appeared to decrease with the number of cycles with a concomitant increase in M (clearest at 300 K) toward the initial value as the number of cycles increased.

We believe that the observed $M(T)$ behavior can be attributed to nonequilibrium processes induced by heating. To elucidate these processes, OL-HT NPs were annealed at 650 and 900 K to produce OL-HT-650K and OL-HT-900K, respectively. We note that the 2-h annealing time for these derivative samples was much longer than the duration of the heating cycles in Figure 1, allowing us to observe changes in structure and composition more clearly.

Sample crystallinity was characterized by XRD (Figure 2). As-synthesized OL-HT NPs exhibited an XRD pattern with high background and broad peaks typical for nanopowders. In contrast, distinctly sharper diffraction peaks were observed for OL-HT-900K, indicating enhanced crystallinity and enlarged particle size produced by annealing at 900 K. According to the phase analysis, all three samples resembled single-phase magnetite with cubic inverse-spinel type structure (ICDD no. 00-019-629, $Fd\bar{3}m$). A lattice shift was observed as the annealing temperature was increased to 900 K; that is, the peaks shifted to a lower angle, reflecting a larger d spacing. The unit-cell parameter a was established to be 8.381(1), 8.378(1), and 8.4007(4) Å for OL-HT, OL-HT-650K, and OL-HT-900K, respectively, where the latter value is in good agreement

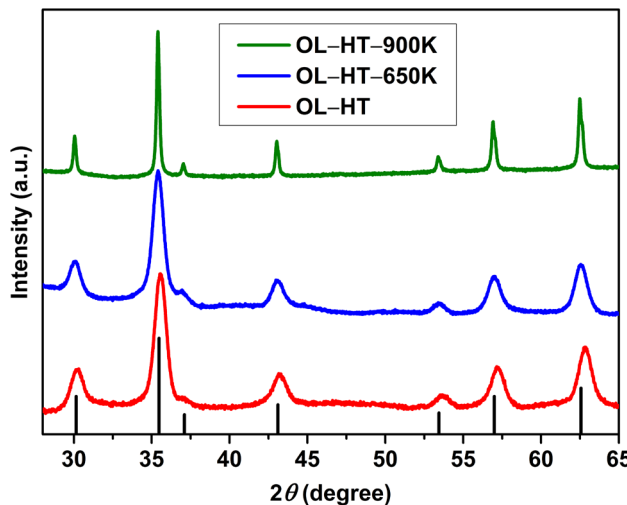


Figure 2. XRD patterns collected from magnetite NPs as-synthesized and after annealing at 650 or 900 K. Tick marks below the patterns correspond to the positions of the Bragg reflections expected for magnetite with a cubic inverse-spinel structure (ICDD no. 00-019-629).

with the unit-cell parameter of bulk Fe_3O_4 (8.396 Å). This trend among a values is unusual, as high-temperature annealing of oxide NPs often results in solvent removal and annihilation of defects, thus leading to decreasing a values.^{10,15} In contrast, a substantial increase in the unit cell was observed for our magnetite NPs. A possible reason for this increase is a partial reduction of Fe^{3+} into Fe^{2+} , which has a larger ionic radius (0.64 Å vs 0.78 Å).¹⁶

Iron oxide phases before and after annealing were investigated by Raman scattering (Figure 3; Table S1, SI).

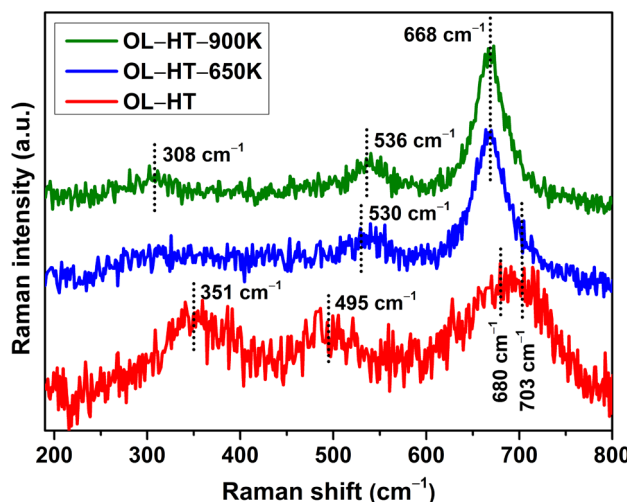


Figure 3. Raman scattering data collected from magnetite NPs as-synthesized and after annealing at 650 and 900 K. Dotted lines mark the positions of resolved bands.

The coexistence of magnetite with an admixture of maghemite ($\gamma\text{-Fe}_2\text{O}_3$) is evidenced by Lorentzian fitting of the Raman data for **OL-HT** NPs. Specifically, the prominent bands centered at 680 and 703 cm^{-1} in the Raman spectrum of **OL-HT** are assigned to A_{1g} phonon modes of Fe_3O_4 and $\gamma\text{-Fe}_2\text{O}_3$, respectively.¹⁷ Additional expected bands representing T_{2g} and E_g phonon modes of $\gamma\text{-Fe}_2\text{O}_3$ can also be observed in

the low-wavenumber region (351 and 495 cm^{-1}). The Raman spectra of the two annealed samples are similar to each other, and the set of observed bands and spectrum features agrees with the Raman data reported for phase-pure Fe_3O_4 .¹⁷ Notably, Lorentzian fitting of the Raman data suggested that the annealed samples contained contributions from $\gamma\text{-Fe}_2\text{O}_3$; however, the magnitudes of the contributions were very low, as one can see from the large values of the intensity and peak area ratios of the respective Fe_3O_4 and $\gamma\text{-Fe}_2\text{O}_3$ prominent A_{1g} bands (Table S1, SI). Thus, Raman scattering points to a minor admixture of $\gamma\text{-Fe}_2\text{O}_3$ in both annealed products. Notably, the A_{1g} mode of Fe_3O_4 , seen in the Raman spectrum of as-synthesized **OL-HT** at 680 cm^{-1} , shifted to lower wavenumbers (668 cm^{-1}) upon annealing. Additionally, the width of this band decreased from 90 cm^{-1} for **OL-HT** to 38 cm^{-1} for **OL-HT-900K**, indicating that the crystalline quality of magnetite increased with annealing, in good agreement with the XRD data.

TEM analysis was applied to investigate the evolution of the structure, size, and morphology of the Fe_3O_4 NPs with annealing. Figure 4a shows a typical low-magnification bright-

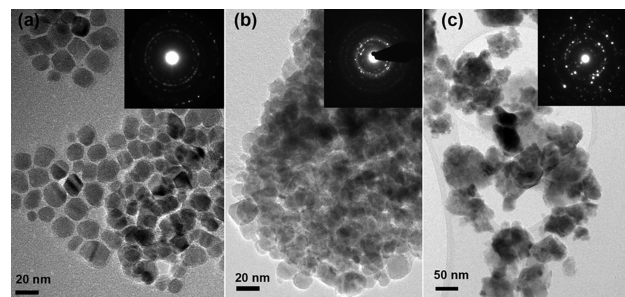


Figure 4. Low-magnification BF TEM images of NPs before and after annealing. NP morphologies and (insets) corresponding ring ED patterns show microstructural changes from (a) as-synthesized NPs to derived NPs annealed at (b) 650 and (c) 900 K.

field (BF) TEM image of **OL-HT**. The average size of the NPs was around 20 ± 3 nm. We note that all of the as-synthesized **OL-HT** NPs were spatially well-separated by the OL capping shells (Figure 4a). In contrast, objects of roughly the same size as **OL-HT** NPs in Figure 4a became aggregated in the annealed **OL-HT-650K** (Figure 4b). Presumably, after thermally induced removal of the OL capping at 650 K, the NPs fused to reduce their surface and interfacial energies, forming aggregates. At the yet higher annealing temperature used for **OL-HT-900K**, NP sintering occurred, resulting in the formation of bulky magnetite products with a typical size of crystallites from 50 to 100 nm (Figures 4c and S1, SI). Electron diffraction (ED) revealed high crystallinity of all of the products, in agreement with the XRD results. The corresponding ED patterns (insets in Figure 4) can be completely indexed based on the cubic $Fd\bar{3}m$ magnetite structure, using the unit-cell parameters determined by XRD.

Figures 5a and S2 (SI) show representative BF HRTEM images of **OL-HT**, wherein the NP surface is terminated with columns of iron atoms and some of the particles exhibit defects, in agreement with our previous report.¹² Annealing at 650 K removed these structural defects, as seen in high-resolution HAADF-STEM images viewed along [001] and [111] zone axes (Figure 5b,c). In contrast to the highly crystalline surfaces of the **OL-HT** NPs, however, a 0.7–1.1-nm-thick amorphous

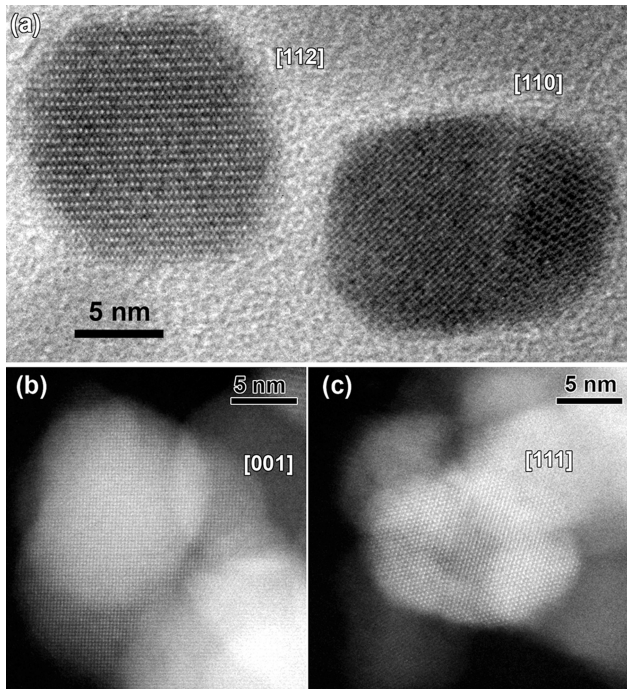


Figure 5. (a) [112] and [110] BF HRTEM images of the as-synthesized OL-HT magnetite NPs and (b,c) HAADF-STEM images of the annealed OL-HT-650K sample with magnetite NPs along the (b) [001] and (c) [111] zone axes.

surface layer was clearly visible on the OL-HT-650K NPs in Figure 6 (top panel). STEM-EDX data (Figure 6, bottom panel) suggest that this layer most likely consisted of carbonaceous residues that formed during thermal decomposition of the OL capping.

Figure 7 shows ^{57}Fe Mössbauer spectra of the as-synthesized OL-HT NPs and the annealed OL-HT-650K and OL-HT-900K derivatives; all of the hyperfine parameters extracted from the measurements are summarized in Table S2 (SI).

The room-temperature Mössbauer spectrum of as-synthesized OL-HT NPs exhibits four components, one of which is very broad, probably due to the superparamagnetic effect.^{18–20} These component widths make the fitting of the Mössbauer spectrum ambiguous; therefore, this sample was measured at 80 K to obtain sharper spectral lines. The 80 K spectrum also has four components, namely, Q_1 , Q_2 , Q_3 , and Q_4 . Three components, Q_1 , Q_3 , and Q_4 , have centroid shift (δ) values ranging from 0.372 to 0.515 mm/s (Table S2, SI). These values are characteristic for Fe^{3+} , taking into account the second-order Doppler shift. The forth component, Q_2 , has a δ value of 0.856 mm/s (Table S2, SI); such a high value of the centroid shift can be assigned to Fe^{2+} . The measurements were performed below the charge-ordering Verwey transition,²¹ which is 120 K for Fe_3O_4 ; therefore, a separate signal coming from Fe^{2+} in the Fe_3O_4 octahedral site is expected, in accordance with the results of Evans and Hafner.²² The observed Fe^{2+} component had an intensity of 12% instead of 33% expected for phase-pure bulk Fe_3O_4 , where the $\text{Fe}^{3+}/\text{Fe}^{2+}$ ratio is 2:1. Thus, the as-synthesized sample contained ca. 36% magnetite and 64% of an Fe^{3+} phase, which was presumably maghemite $\gamma\text{-Fe}_2\text{O}_3$, as indicated by Raman scattering (Figure 3).

In contrast to OL-HT, derivative sample OL-HT-650K annealed at 650 K produced a room-temperature Mössbauer spectrum without superparamagnetic broadening of its sharp

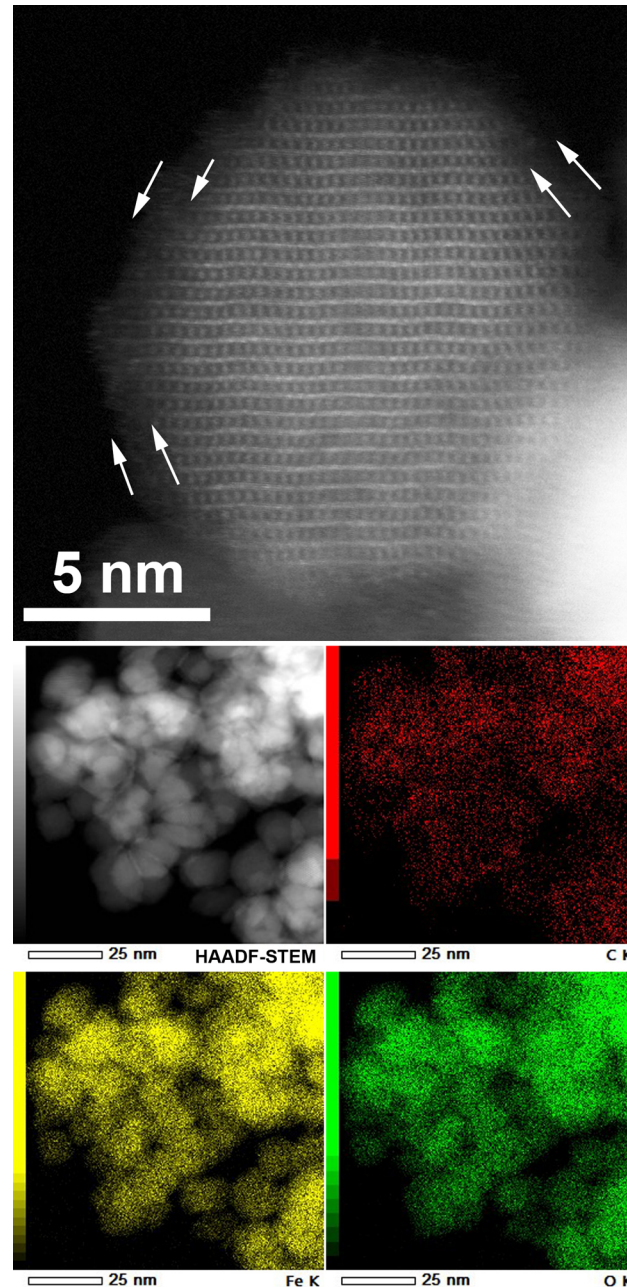


Figure 6. (Top) HAADF-STEM image of an annealed OL-HT-650K NP. Arrows mark an apparent carbonaceous layer at the edge of the NP. (Bottom) HAADF-STEM image of OL-HT-650K NPs, together with the corresponding STEM-EDX maps showing C, Fe, and O distributions.

lines, which was fitted by four components (Table S2, SI). The Q_2 component has a δ value of 0.635 mm/s, which is characteristic for Fe^{2+} , that is, the averaged $\text{Fe}^{3+}/\text{Fe}^{2+}$ signal from iron atoms in the octahedral sites of magnetite. The measurement was performed above the Verwey transition temperature; therefore, no charge ordering or separation of Fe^{2+} and Fe^{3+} in the octahedral positions was expected. The intensity of this combined signal was 36%, indicating that half of it, 18%, was from Fe^{2+} . Hence, the Mössbauer data indicate that annealing at 650 K led to the reduction of part of the Fe^{3+} in the as-synthesized sample to Fe^{2+} , increasing the total fraction of Fe_3O_4 to 54%.

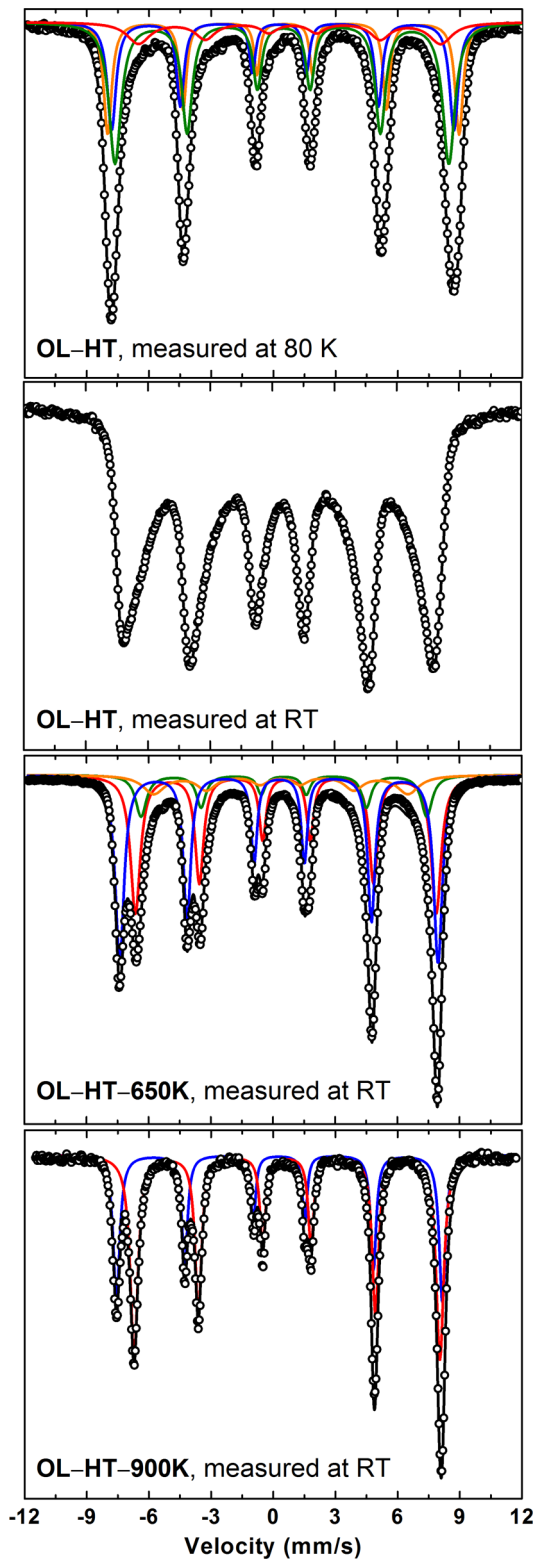


Figure 7. Comparison of the Mössbauer spectra of as-synthesized **OL-HT** and annealed **OL-HT-650K** and **OL-HT-900K** samples collected at room temperature (and at 80 K for **OL-HT**). Experimental data, circles; calculated spectrum, black line; Fe^{2+} or $\text{Fe}^{2.5+}$ component, red line; Fe^{3+} components: blue, green, and orange lines.

Annealing of the as-synthesized NPs at 900 K resulted in almost complete elimination of the putative $\gamma\text{-Fe}_2\text{O}_3$ phase. The Mössbauer spectrum of **OL-HT-900K** was fitted with only two

components, Q_1 and Q_2 (Table S2, SI). Component Q_2 has a δ value of 0.660 mm/s and is from $\text{Fe}^{+2.5}$ in the octahedral site. The intensity of this component is 62%, which is close to the 67% value expected for pure Fe_3O_4 . The slightly lower intensity of Q_2 indicates that a small excess, ca. 7%, of Fe^{3+} is still present in the sample.

4. DISCUSSION

The two striking phenomena we observed in the magnetic properties of our NPs at high temperature—a dip in $M(T)$ at ca. 602 K in the first heating curve and loops in the subsequent cooling/heating $M(T)$ curves in the 500–800 K temperature range—appear to be different in nature; therefore, the first heating curve should be considered separately from the subsequent ones.

4.1. Origin of the Dip in $M(T)$. The temperature at which the dip in $M(T)$ was observed, 602 K, matches very well the decomposition temperature of the OL ligand shell, 605 K, as detected by a combination of TGA/DSC and mass spectrometry.^{11,12} We hypothesize that the decomposition of the organic coating has a significant impact on the magnetic properties of NPs. To verify this assumption, we used a hydrothermal method to synthesize a reference sample of ligand-free magnetite NPs. This reference material did not feature a dip in $M(T)$ upon heating (black curve, Figure 8a), confirming that the dip observed for OL-functionalized NPs is associated with the presence of the organic capping ligands and, more specifically, with their thermal decomposition, based on the temperature at which the dip occurred (Figures 1 and 8b). Therefore, we deduce that the dip in $M(T)$ is most likely related to changes in the composition or oxidation state of the iron oxide on the surface of the NPs, as a consequence of the decomposition of the organic shell.

Looking for evidence of these changes in composition or oxidation state of the iron oxide, in fact, motivated our choice of the 650 K annealing temperature for the **OL-HT-650K** derivative sample. Our Raman analysis suggested the $\gamma\text{-Fe}_2\text{O}_3$ phase in as-synthesized **OL-HT** to be the most likely candidate for undergoing the transformation upon heating. Indeed, after the sample had been annealed at 650 K, the contribution of $\gamma\text{-Fe}_2\text{O}_3$ became quite small (compare **OL-HT** and **OL-HT-650K** in Figure 3 and Table S1, SI). Mössbauer analysis confirmed that, after the sample had been annealed at 650 K, the content of Fe^{2+} increased at the expense of Fe^{3+} (Figure 7; Table S2, SI). Thus, both Raman and Mössbauer analyses point to the reduction of the Fe^{3+} -rich surface layer, which is characteristic of as-synthesized **OL-HT** NPs,¹² as the main change in iron oxide composition of **OL-HT** upon annealing at 650 K.

The in situ reducing agent^{23,24} for this apparent Fe^{3+} reduction is suggested by its connection to the presence and thermal decomposition of the organic capping ligands, as deduced from the $M(T)$ features (Figure 8) and from carbonaceous residues observed by HAADF-STEM and STEM-EDX (Figure 6). The reduction did not take place in the absence of the putative reducing agent in ligand-free NPs, which did not exhibit the dip feature (black curve in Figure 8a).

The following model then emerges to explain the dip in $M(T)$ during the first heating of as-synthesized **OL-HT** NPs: As-synthesized NPs contain a significant excess of Fe^{3+} both in the core and on the surface of the particles, forming $\text{Fe}_3\text{O}_4\text{-}\gamma\text{-Fe}_2\text{O}_3$ solid solutions.¹² Upon the first heating above ca. 600 K, the OL ligands decompose, and the carbonaceous product of

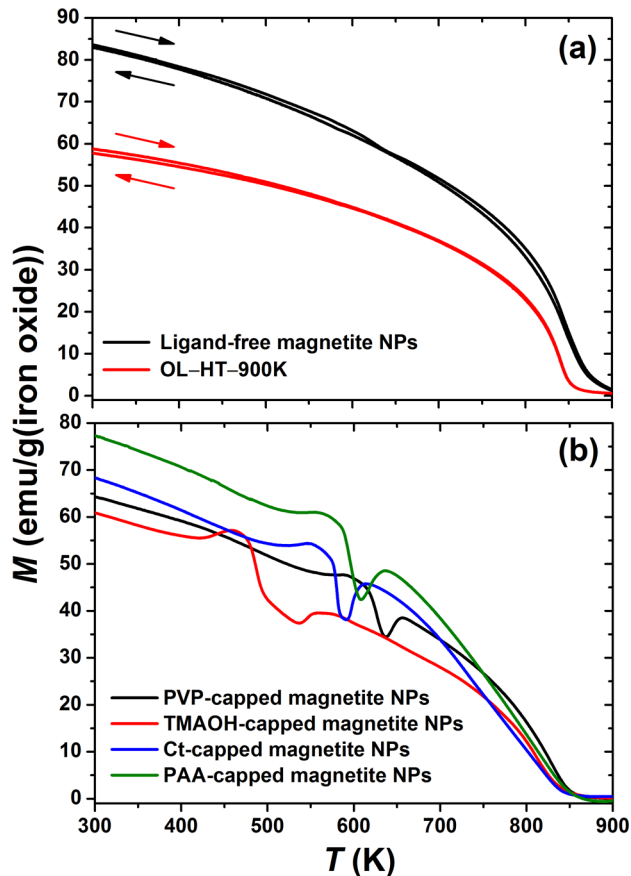


Figure 8. (a) One heating–cooling $M(T)$ cycle for a reference magnetite sample synthesized without organic coating (ligand-free magnetite) and for an annealed sample (OL-HT-900K). (b) $M(T)$ data for model magnetite NPs functionalized with different organic capping ligands: poly(vinylpyrrolidone) (PVP), tetramethylammonium hydroxide (TMAOH), citrate (Ct), and poly(acrylic acid) (PAA). All data were measured in a 10 kOe field.

that decomposition induces the *in situ* reduction of part of the excess Fe^{3+} on the NP surfaces. Although formation of secondary metallic iron, iron carbide, or oxo-carbide phases can be expected as a result of a carbon-induced reduction, our detailed characterization did not reveal any major phase other than magnetite. Accordingly, the reduction and associated magnetite-phase stabilization must produce the dip in the magnetization. In particular, during the reduction, the NPs likely exhibit chemical disorder associated with the migration and redistribution of O and Fe ions. This disorder leads to the frustration of Fe–O–Fe superexchange interactions, generating a dip in $M(T)$ until the reduction is complete.^{3,9,10,25}

The remaining excess of Fe^{3+} detected by Mössbauer spectroscopy in OL-HT-650K (Figure 7; Table S2, SI) was likely situated in the core of the particles. Indirect evidence of this Fe^{3+} localization is provided by minimal changes in the unit-cell parameters (and, therefore, in the structure of NP cores) upon annealing at 650 K (Figure 2). We note that, even in the annealed OL-HT-650K sample, the original NPs were identifiable (Figure 4b), so the *in situ* reduction was largely confined within individual NPs. A temperature of 650 K was thus not sufficient to produce a uniform composition across an entire 20-nm NP. Temperature, rather than heating time, was implicated as the primary limiting factor based on the observation that, during magnetometry measurements, heating

for just a few minutes around 600 K was sufficient to complete the putative reduction reaction on the NP surfaces (completion is inferred from the dip being unique to the initial heating), whereas even the much longer (2-h) annealing of OL-HT-650K did not extend the reaction to NP cores, as indicated above (Figures 2 and 7; Table S2, SI).

4.2. Origin of $M(T)$ Irreversibility. We observed a significant irreversibility in consecutive cooling and heating profiles of $M(T)$ in OL-HT, whereby starting from the second heating–cooling cycle, the M value at 300 K increased after every cycle (cycles 2 and 3 in Figure 1). Our analyses of annealed OL-HT-650K and OL-HT-900K samples by diffraction techniques (XRD in Figure 2 and ED in Figure 4) and Raman scattering (Figure 3) did not reveal any phase transition in the temperature range of the $M(T)$ measurements, but pointed to two types of gradual changes, namely, sintering and equilibration of the Fe_3O_4 composition, as likely explanations for the gradual recovery of M at 300 K.

Owing to their small size, the NPs exhibit a high specific surface area. Structurally, the surface of the NPs is disordered, giving rise to a reasonable quantity of magnetically dead layer on the particle surface. The series of TEM images in Figure 4 clearly indicates that, in the temperature range of our $M(T)$ measurements, NP sintering occurred, promoted by both heating and reducing conditions²⁶ (the latter are discussed in more detail in section 4.1). The gradual increase in the crystallite size of magnetite with sintering is not only evident in the TEM images (Figures 4c and S1, SI) but is also supported by the sharpest peaks in the XRD (Figure 2) and Raman (Figure 3) data for the OL-HT-900K sample annealed at 900 K, that is, at the high-temperature limit of our $M(T)$ measurements. During the sintering, the particles grew, and accordingly, their specific surface area decreased. The overall effect of the magnetically dead layer then diminished, leading to the gradual increase in M .²⁷

Apart from the anticipated sintering-induced size effect, the gradual recovery of M was also tracked down to the uncommon significant change in $\text{Fe}^{3+}/\text{Fe}^{2+}$ ratio with the heat treatment. As discussed above, annealing at 650 K was not sufficient to reach the theoretical Fe_3O_4 stoichiometry of Fe^{3+} and Fe^{2+} across an entire 20-nm NP. Analysis of Mössbauer spectra for OL-HT-900K (Figure 7; Table S2, SI), however, clearly indicates that the larger (50–100-nm) sintered particles produced by annealing at 900 K exhibited a nearly uniform Fe_3O_4 composition. The uniformity of converting the initial excess Fe^{3+} to Fe^{2+} across the entire volume of these larger particles is further indicated by the increase of the unit-cell parameter to the bulk Fe_3O_4 value (Figure 2) after annealing at 900 K, in contrast to the commonly observed reduction in unit-cell parameters in annealed metal oxide NPs.^{10,15} This seemingly simple change in $\text{Fe}^{3+}/\text{Fe}^{2+}$ ratio is deceptive, as the compositional change from ca. 46% to 7% of Fe_2O_3 significantly increased M , judging by the fact that the M_s value of Fe_3O_4 is higher than that of $\gamma\text{-Fe}_2\text{O}_3$.

Thus, both sintering and uncommon equilibration of the Fe_3O_4 composition would contribute to the gradual increase of M in heating–cooling cycles, because M is expected to increase with both larger particle size and improved Fe_3O_4 crystallinity and uniformity. Neither process, however, reached an end point or equilibrium during the short high-temperature phase of each heating–cooling cycle; therefore, divergent $M(T)$ curves depicting loops were produced as the sample gradually approached its end-point configuration. This interpretation is

supported by the nearly reversible $M(T)$ cycle for **OL-HT-900K** (red curve in Figure 8a), which indicates that annealing for 2 h at 900 K was sufficient to complete the sintering of the original NPs and equilibration of the Fe_3O_4 composition throughout the resulting particles. As 900 K was the highest temperature reached in every heating cycle, the **OL-HT-900K** behavior confirms that, in this particular case, heating time rather than temperature was the parameter limiting the extent of NP transformation in each cycle.

4.3. Structure and Composition Inferences and Models. Our extensive analysis of the as-synthesized **OL-HT** NPs combined with measurements of $M(T)$ and of derivative samples annealed at elevated temperatures provide the basis for the following inferences about the structure and composition of **OL-HT** NPs.

Iron oxide in as-synthesized **OL-HT** NPs is best understood as an $\text{Fe}_3\text{O}_4-\gamma\text{-Fe}_2\text{O}_3$ solid solution with excess (beyond Fe_3O_4 stoichiometry) Fe^{3+} distributed throughout the NPs, with indications of a possible enrichment at their surfaces.^{12,28} $\gamma\text{-Fe}_2\text{O}_3$ and Fe_3O_4 have very similar crystal structures. Both powder XRD and (Figure 2) and high-resolution TEM (Figure 5a) indicate that the as-synthesized sample had a cubic inverse-spinel structure, which is also the case for both pure Fe_3O_4 and $\text{Fe}_3\text{O}_4-\gamma\text{-Fe}_2\text{O}_3$ solid solution. Local Mössbauer spectroscopy revealed the elevated Fe^{3+} to Fe^{2+} ratio in **OL-HT** (Figure 7; Table S2, SI); the associated $\gamma\text{-Fe}_2\text{O}_3$ phase was detected by Raman scattering (Figure 3).

Indirect evidence of a possible enhancement of M by the capping OL ligands of **OL-HT** NPs comes from a comparison of the initial M values for **OL-HT** (Figure 1) and **OL-HT-900K** (red curve in Figure 8a). As discussed above, both the increased size of the particles in **OL-HT-900K** and its predominantly magnetite composition should increase the M value for this material. However, the initial M value at room temperature for **OL-HT** NPs before thermal treatment was actually slightly higher than the M value at room temperature for **OL-HT-900K**, despite the smaller NP size and structural/compositional imperfection of magnetite in **OL-HT**. A higher amount of $\gamma\text{-Fe}_2\text{O}_3$ in **OL-HT** does not justify this difference in M , as Fe_3O_4 has an even higher magnetic moment than $\gamma\text{-Fe}_2\text{O}_3$. Ligand enhancement of M in **OL-HT** NPs provides a possible interpretation of this apparent discrepancy.

The above inferences provide illustrations of how investigating the properties of magnetic NPs at elevated temperatures can provide insights into the structure and composition of as-synthesized NPs. These illustrations reinforce our prospective that high-temperature measurements can be useful for NPs that are intended for room-temperature applications. An example of extending this analytical concept to investigating NPs capped with common organic ligands is shown in Figure 8b. For each model colloidal magnetite NP, the dip in $M(T)$ is observed at a specific temperature that closely corresponds (within ≤ 3 K) to the sharp step in thermal decomposition of the capping ligands: poly(vinylpyrrolidone),²⁹ tetramethylammonium hydroxide,³⁰ citrate,³¹ and poly(acrylic acid).^{11,12} Observation of a dip in $M(T)$ at a characteristic temperature, therefore, can be used to confirm the identities of these common capping ligands.

5. CONCLUSIONS

We have observed complex irreversible behavior of magnetization for OL-capped magnetite nanoparticles upon thermal cycling in the 300–900 K temperature range. Two prominent features of $M(T)$ curves for these NPs are (1) a dip in $M(T)$

during the initial heating and (2) an irreversibility of heating–cooling curves, producing loops in subsequent cycles. Both features are related to the thermal decomposition of the OL capping ligands. The dip in $M(T)$ is due to the reduction of overoxidized NP surfaces by carbonaceous decomposition products. The $M(T)$ irreversibility results from gradual NP sintering and uncommon compositional equilibration after reduction of overoxidized NP cores, both of which are enabled after thermal decomposition of the capping ligands.

Our analysis of as-synthesized NPs, combined with measurements of $M(T)$ and of derivative samples annealed at elevated temperatures, indicates that iron oxide in as-synthesized colloids is best understood as an $\text{Fe}_3\text{O}_4-\gamma\text{-Fe}_2\text{O}_3$ solid solution with excess Fe^{3+} present both in the NP cores and on their overoxidized surfaces. We also found indirect evidence of the M enhancement by capping ligands in as-synthesized NPs.

The novel analytical methodology demonstrated in this work can be readily extended to structural and compositional analyses of magnetic nanomaterials. Reversible $M(T)$ curves indicate uniform structure and composition, as well as a lack of organic capping ligands. Conversely, characteristic features in irreversible $M(T)$ curves provide insights into the nature of structural or compositional uniformity, as well as the identity of the organic capping ligands.

■ ASSOCIATED CONTENT

S Supporting Information

Additional synthesis, characterization, Raman scattering, Mössbauer spectroscopy, and electron microscopy data. This material is available free of charge via the Internet at <http://pubs.acs.org>.

■ AUTHOR INFORMATION

Corresponding Author

*E-mail: yury.kolenko@inl.int.

Notes

The authors declare no competing financial interest.

■ ACKNOWLEDGMENTS

We thank Dr. L. M. Salonen and Prof. P. Freitas for helpful discussions, as well as J. T. Greenfield for sample preparation for Mössbauer spectroscopy. We also acknowledge the European Regional Development Fund (ON.2 – O Novo Norte Program), the EU FP7 Cooperation Program through the NMP theme (Grant 314212), and the InveNNta project financed by the EU Programme for Cross-border Cooperation: Spain–Portugal (POCTEP 2007–2013) for supporting this work. The Mössbauer facility was supported by the NIH (Grant 1S10RR023656-01A1). E.C.-A. acknowledges the I2C Plan (Xunta de Galicia, Spain) for a postdoctoral fellowship. O.I.L. gratefully acknowledges the financial support of the Ministry of Education and Science of the Russian Federation within the framework of the Increase Competitiveness Program of NUST “MISIS” (Grant K3-2014-021).

■ REFERENCES

- Gao, J. H.; Gu, H. W.; Xu, B. Multifunctional Magnetic Nanoparticles: Design, Synthesis, and Biomedical Applications. *Acc. Chem. Res.* **2009**, 42, 1097–1107.
- Zhang, F.; Lees, E.; Amin, F.; Gil, P. R.; Yang, F.; Mulvaney, P.; Parak, W. J. Polymer-Coated Nanoparticles: A Universal Tool for Biolabelling Experiments. *Small* **2011**, 7, 3113–3127.

- (3) Guardia, P.; Batlle-Brugal, B.; Roca, A. G.; Iglesias, O.; Morales, M. P.; Serna, C. J.; Labarta, A.; Batlle, X. Surfactant Effects in Magnetite Nanoparticles of Controlled Size. *J. Magn. Magn. Mater.* **2007**, *316*, E756–E759.
- (4) Guardia, P.; Labarta, A.; Batlle, X. Tuning the Size, the Shape, and the Magnetic Properties of Iron Oxide Nanoparticles. *J. Phys. Chem. C* **2011**, *115*, 390–396.
- (5) McDannald, A.; Staruch, M.; Jain, M. Surface Contributions to the Alternating Current and Direct Current Magnetic Properties of Oleic Acid Coated CoFe_2O_4 Nanoparticles. *J. Appl. Phys.* **2012**, *112*.
- (6) Winkler, E.; Zysler, R. D.; Mansilla, M. V.; Fiorani, D.; Rinaldi, D.; Vasilakaki, M.; Trohidou, K. N. Surface Spin-Glass Freezing in Interacting Core–Shell NiO Nanoparticles. *Nanotechnology* **2008**, *19*, 185702.
- (7) Levy, D.; Giustetto, R.; Hoser, A. Structure of Magnetite (Fe_3O_4) above the Curie Temperature: A Cation Ordering Study. *Phys. Chem. Miner.* **2012**, *39*, 169–176.
- (8) Desautels, R. D.; van Lierop, J.; Cadogan, J. M. Disproportionation of Cobalt Ferrite Nanoparticles Upon Annealing. *J. Phys. Conf. Ser.* **2010**, *217*, 012105.
- (9) Huang, Y. H.; Karppinen, M.; Yamauchi, H.; Goodenough, J. B. Systematic Studies on Effects of Cationic Ordering on Structural and Magnetic Properties in $\text{Sr}_2\text{FeMoO}_6$. *Phys. Rev. B* **2006**, *73*.
- (10) Ray, S.; Kolen'ko, Y. V.; Kovnir, K. A.; Lebedev, O. I.; Turner, S.; Chakraborty, T.; Erni, R.; Watanabe, T.; Van Tendeloo, G.; Yoshimura, M.; Itoh, M. Defect Controlled Room Temperature Ferromagnetism in Co-Doped Barium Titanate Nanocrystals. *Nanotechnology* **2012**, *23*, 025702.
- (11) Rodriguez, C.; Bañobre-López, M.; Kolen'ko, Y. V.; Rodriguez, B.; Freitas, P.; Rivas, J. Magnetization Drop at High Temperature in Oleic Acid-Coated Magnetite Nanoparticles. *IEEE Trans. Magn.* **2012**, *48*, 3307–3310.
- (12) Kolen'ko, Y. V.; Bañobre-López, M.; Rodríguez-Abreu, C.; Carbó-Argibay, E.; Salsman, A.; Piñeiro-Redondo, Y.; Cerqueira, M. F.; Petrovych, D. Y.; Kovnir, K.; Lebedev, O. I.; Rivas, J. Large-Scale Synthesis of Colloidal Fe_3O_4 Nanoparticles Exhibiting High Heating Efficiency in Magnetic Hyperthermia. *J. Phys. Chem. C* **2014**, *118*, 8691–8701.
- (13) Akselrud, L. G.; Zavalii, P. Y.; Grin, Y. N.; Pecharsky, V. K.; Baumgartner, B.; Wolfel, E. Use of the CSD Program Package for Structure Determination from Powder Data. *Mater. Sci. Forum* **1993**, *133–136*, 335–340.
- (14) Lagarec, K.; Rancourt, D. C. RECOIL. *Mössbauer Spectral Analysis Software for Windows*, version 1.0; Department of Physics, University of Ottawa: Ottawa, Canada, 1998.
- (15) Kolen'ko, Y. V.; Kovnir, K. A.; Neira, I. S.; Taniguchi, T.; Ishigaki, T.; Watanabe, T.; Sakamoto, N.; Yoshimura, M. A Novel, Controlled, and High-Yield Solvothermal Drying Route to Nanosized Barium Titanate Powders. *J. Phys. Chem. C* **2007**, *111*, 7306–7318.
- (16) Shannon, R. D. Revised Effective Ionic Radii and Systematic Studies of Interatomic Distances in Halides and Chalcogenides. *Acta Crystallogr. A* **1976**, *32*, 751–767.
- (17) Jubb, A. M.; Allen, H. C. Vibrational Spectroscopic Characterization of Hematite, Maghemite, and Magnetite Thin Films Produced by Vapor Deposition. *ACS Appl. Mater. Interfaces* **2010**, *2*, 2804–2812.
- (18) Häggström, L.; Kamali, S.; Ericsson, T.; Nordblad, P.; Ahniyaz, A.; Bergström, L. Mössbauer and Magnetization Studies of Iron Oxide Nanocrystals. *Hyperfine Interact.* **2008**, *183*, 49–53.
- (19) Mørup, S. Magnetic Hyperfine Splitting in Mössbauer-Spectra of Micro-Crystals. *J. Magn. Magn. Mater.* **1983**, *37*, 39–50.
- (20) Kamali, S.; Ericsson, T.; Wäppling, R. Characterization of Iron Oxide Nanoparticles by Mössbauer Spectroscopy. *Thin Solid Films* **2006**, *515*, 721–723.
- (21) Verwey, E. J. W. Electronic Conduction of Magnetite (Fe_3O_4) and Its Transition Point at Low Temperatures. *Nature* **1939**, *144*, 327–328.
- (22) Evans, B. J.; Hafner, S. S. ^{57}Fe Hyperfine Fields in Magnetite (Fe_3O_4). *J. Appl. Phys.* **1969**, *40*, 1411–1413.
- (23) Julien, C. M.; Manger, A.; Ait-Salah, A.; Massot, M.; Gendron, F.; Zaghib, K. Nanoscopic Scale Studies of LiFePO_4 as Cathode Material in Lithium-Ion Batteries for HEV Application. *Ionics* **2007**, *13*, 395–411.
- (24) Kolen'ko, Y. V.; Amakawa, K.; d'Alnoncourt, R. N.; Girgsdies, F.; Weinberg, G.; Schlogl, R.; Trunschke, A. Unusual Phase Evolution in MoVTeNb Oxide Catalysts Prepared by a Novel Acrylamide-Gelation Route. *ChemCatChem* **2012**, *4*, 495–503.
- (25) Belayachi, A.; Loudghiri, E.; El Yamani, M.; Nogues, M.; Dormann, J. L.; Taibi, M. Unusual Magnetic Behavior in $\text{LaFe}_{1-x}\text{Cr}_x\text{O}_3$. *Ann. Chim.: Sci. Mater.* **1998**, *23*, 297–300.
- (26) Xia, W.; Su, D. S.; Birkner, A.; Ruppel, L.; Wang, Y. M.; Woll, C.; Qian, J.; Liang, C. H.; Marginean, G.; Brandl, W.; Muhler, M. Chemical Vapor Deposition and Synthesis on Carbon Nanofibers: Sintering of Ferrocene-Derived Supported Iron Nanoparticles and the Catalytic Growth of Secondary Carbon Nanofibers. *Chem. Mater.* **2005**, *17*, 5737–5742.
- (27) Dutta, P.; Pai, S.; Seehra, M. S.; Shah, N.; Huffman, G. P. Size Dependence of Magnetic Parameters and Surface Disorder in Magnetite Nanoparticles. *J. Appl. Phys.* **2009**, *105*, 07B501.
- (28) Schmidbauer, E.; Keller, M. Magnetic Hysteresis Properties, Mössbauer Spectra and Structural Data of Spherical 250 nm Particles of Solid Solutions $\text{Fe}_3\text{O}_4-\gamma\text{-Fe}_2\text{O}_3$. *J. Magn. Magn. Mater.* **2006**, *297*, 107–117.
- (29) Johnson, N. J. J.; Sangeetha, N. M.; Boyer, J. C.; van Veggel, F. C. J. M. Facile Ligand-Exchange with Polyvinylpyrrolidone and Subsequent Silica Coating of Hydrophobic Upconverting $\beta\text{-NaYF}_4:\text{Yb}^{3+}/\text{Er}^{3+}$ Nanoparticles. *Nanoscale* **2010**, *2*, 771–777.
- (30) Salgueirino-Maceira, V.; Correa-Duarte, M. A.; Farle, M. Manipulation of Chemically Synthesized FePt Nanoparticles in Water: Core–Shell Silica/FePt Nanocomposites. *Small* **2005**, *1*, 1073–1076.
- (31) Parracino, A.; Gajula, G. P.; di Gennaro, A. K.; Correia, M.; Neves-Petersen, M. T.; Rafaelsen, J.; Petersen, S. B. Photonic Immobilization of BSA for Nanobiomedical Applications: Creation of High Density Microarrays and Superparamagnetic Bioconjugates. *Biotechnol. Bioeng.* **2011**, *108*, 999–1010.